Self-Sensing, Ultralight, and Conductive 3D Graphene/Iron Oxide Aerogel Elastomer Deformable in a Magnetic Field

Xiang Xu,[†,‡] Hui Li,[*,†,‡] Qiangqiang Zhang,[†,‡] Han Hu,[§] Zongbin Zhao,[§] Jihao Li,[∥] Jingye Li,[∥] Yu Qiao,[⊥] and Yury Gogotsi[*,§,#]

[†]Key Lab of Structures Dynamic Behavior and Control of the Ministry of Education and [‡]Center of Structural Health Monitoring and Control, School of Civil Engineering, Harbin Institute of Technology, Harbin, 150090, People's Republic of China, [§]Liaoning Key Lab for Energy Materials and Chemical Engineering, State Key Lab of Fine Chemicals, Dalian University of Technology, Dalian 116024, People's Republic of China, [∥]TMSR Research Center and CAS Key Lab of Nuclear Radiation and Nuclear Energy Technology, Shanghai Institute of Applied Physics, Chinese Academy of Sciences, Shanghai, 201800, People's Republic of China, [⊥]Department of Structural Engineering, University of California—San Diego, La Jolla, California 92093, United States, and [#]Department of Materials Science and Engineering and A.J. Drexel Nanotechnology Institute, Drexel University, 3141 Chestnut Street, Philadelphia, Pennsylvania 19104, United States

ABSTRACT Three-dimensional (3D) graphene aerogels (GA) show promise for applications in supercapacitors, electrode materials, gas sensors, and oil absorption due to their high porosity, mechanical strength, and electrical conductivity. However, the control, actuation, and response properties of graphene aerogels have not been well studied. In this paper, we synthesized 3D graphene aerogels decorated with Fe_3O_4 nanoparticles (Fe_3O_4/GA) by self-assembly of graphene with simultaneous decoration by Fe_3O_4 nanoparticles using a modified hydrothermal reduction process. The aerogels exhibit up to 52% reversible magnetic field-induced strain and strain-dependent electrical resistance that can be used to monitor the degree of compression/stretching of the material. The density of Fe_3O_4/GA is only about 5.8 mg cm^{-3}, making it an ultralight magnetic elastomer with potential applications in self-sensing soft actuators, microsensors, microswitches, and environmental remediation.

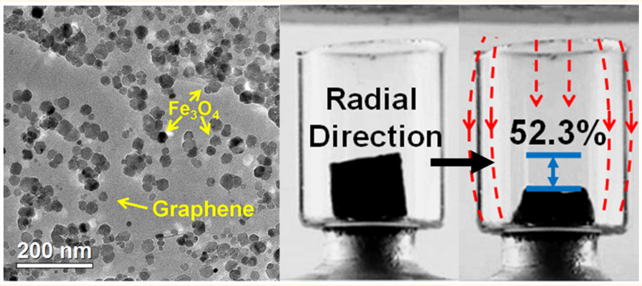

KEYWORDS: graphene aerogel · iron oxide · magnetic field-induced strain · strain-dependent electrical resistance

Three-dimensional (3D) carbon-based metamaterials, such as arrays, foams, sponges, and aerogels of controlled architectures, have recently attracted great attention due to their ultralight weight, high specific surface area, excellent electrical conductivity, and mechanical strength.[1−5] These porous carbons, composed of one-dimensional (1D) carbon nanotubes (CNTs) or two-dimensional (2D) graphenes, demonstrate promise in a wide variety of fields, including energy storage, sensors, catalysis, and environmental science and engineering.[6−17] Compared with a CNT monolith, graphene-based metamaterials, specifically graphene aerogels (GA), tend to have a much lower density (0.16 mg cm^{-3}),[18] higher compressibility (90%),[19] and good electrical conductivity (10 S cm^{-1}).[20] A number of processing techniques, such as hydrothermal reduction,[6,21] chemical reduction,[22−25] organic functionalization,[26] chemical vapor deposition (CVD),[20] electrochemical synthesis,[27] and ice crystal templating,[28] have been used to fabricate high-performance GA. Among these approaches, chemical reduction is an attractive method, as it requires relatively mild processing conditions by using various reducing agents ($NaHSO_3$, Na_2S, vitamin C, HI, ferrous ions, ethylenediamine, *etc.*);[19,22] meanwhile graphene oxides (GO) can be integrated into monolithic aerogels using a self-assembly process.

The excellent mechanical and electronic properties of GA can be further improved by using nanoparticles to form multifunctional 3D networks. A few examples include magnetic graphene/iron oxide aerogels for battery anodes,[29,30] oils/heavy metal ion absorption,[31] and oxygen reduction reaction;[32,33] nickel nanoparticle/graphene aerogels for

* Address correspondence to lihui@hit.edu.cn.

Received for review December 28, 2014 and accepted March 19, 2015.

10.1021/nn507426u

ethanol fuel cells;[34] graphene-carbon sphere hybrid aerogels decorated with silver nanoparticles for catalytic reduction of 4-nitrophenol;[35] nitrogen-doped activated graphene aerogels/gold nanoparticles for electroanalytical analysis,[36] and GA-supported SnO_2 nanoparticles for detection of NO_2.[37]

The research community mainly focused on the improvement of the mechanical, electronic, and absorption properties of 3D GA. However, the controllability, actuation, and dynamic response of GA, which are of critical importance for applications, have received little attention, inspiring this study.

Typical magnetic elastomers, which are being tested as soft actuators, as microsensors in tissue engineering, and for drug delivery and release,[38−42] consist of magnetic nanoparticles and a compliant matrix. Some examples include magnetic hydrogels and magnetic silicones, which have recently drawn increasing attention due to their fast response, large actuation, and possibility of wireless control.[43−50] The "bottlenecks" of magnetic elastomers are the poor recovery after compression and the aggregation of magnetic nanoparticles.

Our objective was to develop an ultralight, conductive, and magnetically responsive 3D GA with outstanding actuation ability and dynamic response, allowing an electrical control over its deformation. In the current study, 3D magnetic Fe_3O_4 nanoparticles decorating graphene aerogels (Fe_3O_4/GA) were synthesized *via* an *in situ* self-assembly of graphene, by a modified hydrothermal reduction of graphene oxide in water in the presence of Fe_3O_4 nanoparticles. The ultralight magnetic elastomer demonstrated excellent field-induced strain and adjustable electrical resistance, which can be exploited for its applications in smart soft actuators, microsensors, and switches, remotely controlled oil absorption, and recycling, to name a few.

RESULTS AND DISCUSSION

The preparation of magnetic Fe_3O_4/GA is illustrated in Figure 1. A GO (Figure 1a) aqueous suspension was first mixed with reducing agent ethylenediamine (EDA) and freshly synthesized Fe_3O_4 nanoparticles. The magnetic responsiveness of Fe_3O_4/GA is a trade-off between network flexibility and magnetic actuation force. A large loading of Fe_3O_4 nanoparticles is required to generate a strong actuation force, but it also leads to an increase in stiffness of Fe_3O_4/GA, which, in turn, tends to reduce the overall strain. The optimal nanoparticle loading was determined as shown in Figures S1−S2 (Supporting Information). After hydrothermal treatment, GO was gradually self-assembled into a hydrogel with simultaneous deposition of Fe_3O_4 nanoparticles (Figure 1b). The role of EDA in the graphene self-assembly process has been discussed in our previous work; it participates in the nucleophilic ring-opening reaction of epoxy groups and reduction of GO.[19] The as-formed hydrogel floated on the surface and the solution was transparent, indicating an efficient adsorption of Fe_3O_4 nanoparticles onto the graphene. The soft hydrogels, fabricated by the modified hydrothermal method, showed a very small volume shrinkage. After lyophilization, black, porous, ultralight (Figure 1c and Figure S3) Fe_3O_4/GA aerogel samples (~17 mm in height, ~10 mm in diameter, and ~7.7 mg in weight) were obtained. Their density was about 5.8 mg cm^{-3} after annealing. This aerogel exhibits excellent magnetic actuation with a magnetic field-induced deformation strain up to 35% along the axial direction and 52% along the radial direction, making it the lightest magnetic elastomer reported so far (Figure 1d,e and Videos S1 and S2).

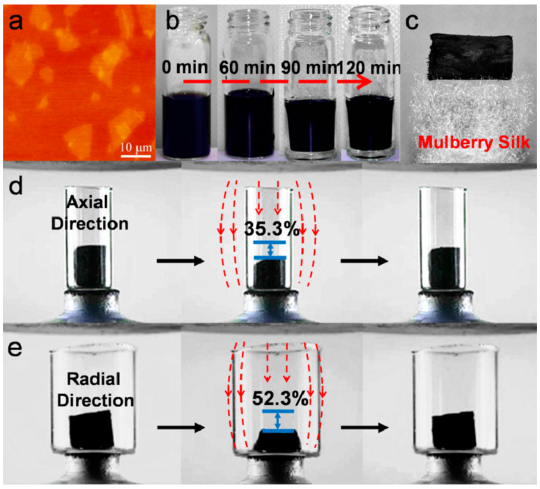

Figure 1. (a) Atomic force microscope (AFM) image of GO particles (bright) deposited on mica (darker background). (b) Illustration of the synthesis (self-assembly) process of Fe_3O_4/GA. (c) Fe_3O_4/GA cylinder with a 5.8 mg cm^{-3} density standing on mulberry silk. (d) Magnetic field-induced compression along the axial direction of Fe_3O_4/GA. (e) Magnetic field-induced compression along the radial direction of Fe_3O_4/GA.

The elemental composition of Fe_3O_4/GA was analyzed by X-ray diffraction (XRD), X-ray photoelectron spectroscopy (XPS), and Raman spectroscopy. Figure 2a shows the XRD patterns of GO, pure graphene aerogel, and Fe_3O_4/GA. For GO, the peak at 7.5° corresponds to the typical diffraction peak[51] with a *d*-spacing of 1.18 nm. However, for GA, a wide diffraction peak appears at about 22°, corresponding to a *d*-spacing of 0.40 nm. Compared to the graphite (002) diffraction peak at 26.5°, this wide peak indicates a restoration of the conjugation of sp^2 regions and $\pi-\pi$ stacking interactions in the cross-linking areas during the graphene self-assembly. However, due to the incomplete reduction of GO, residual functional groups on the graphene sheets slightly enlarge the interlayer spacing, leading to the downshift of this wide peak. For the Fe_3O_4/GA, all the peaks up to 28° can be assigned to the face-centered-cubic crystals of Fe_3O_4 (JCPDS 19-0629), while the wide peak at 23.8° also indicates a

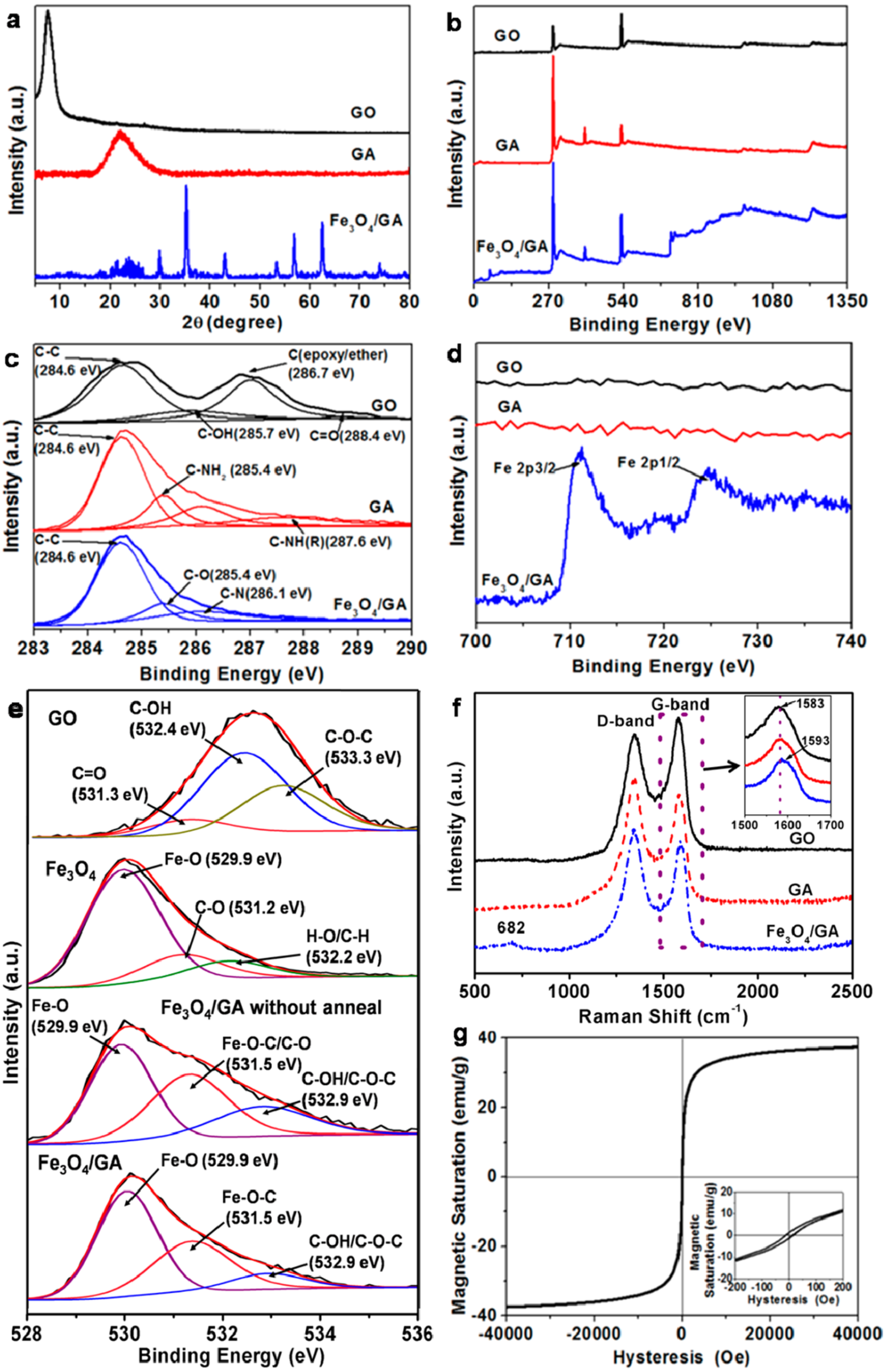

Figure 2. (a) XRD patterns. (b–e) XPS, C 1s spectrum, Fe 2p spectrum, and O 1s spectrum. (f) Raman spectra of GO, GA, and Fe$_3$O$_4$/GA. (g) Hysteresis curve of Fe$_3$O$_4$/GA.

restoration of the conjugation of graphene sp^2 regions during the graphene self-assembly of Fe$_3$O$_4$/GA. Figure 2b shows the wide-scan XPS profiles of GO, GA, and Fe$_3$O$_4$/GA. Only C 1s (284.6 eV) and O 1s (532 eV) peaks can be observed from GO, while an additional N 1s (400 eV) peak can be observed from GA and Fe$_3$O$_4$/GA, which is attributed to the grafted amine groups after EDA-mediated hydrothermal reduction. An obvious Fe 2p (711 eV) peak can be found in Fe$_3$O$_4$/GA, which provides direct evidence of the successful deposition of Fe$_3$O$_4$ nanoparticles onto the graphene network. From the C 1s spectra (Figure 2c), regular peaks of oxygen groups on GO can be clearly observed. After the EDA-mediated hydrothermal reduction, a considerable portion of the oxygen groups (hydroxyl C—OH at 285.7 eV, epoxy C—O at 286.7 eV, and carbonyl C═O at 288.4 eV) are eliminated. From the Fe 2p spectra in Figure 2d, the peaks of Fe 2p$_{3/2}$ and Fe

$2p_{1/2}$ (711.2 and 724.5 eV) in Fe_3O_4/GA are the characteristic positions of Fe_3O_4, demonstrating the presence of Fe_3O_4 nanoparticles in the graphene network. The binding between Fe_3O_4 and GA was studied by XPS (Figure 2e). The O 1s spectrum of GO can be deconvoluted into three peaks, C═O at 531.1 eV, C−OH at 532.4 eV, and C−O−C at 533.3 eV, which are consistent with the C 1s spectrum. The O 1s spectrum of Fe_3O_4 can be deconvoluted into the Fe−O peak at 529.9 eV and some surface-absorbed organic group peaks (C−O at 531.2 eV and O−H/C−H at 532.2 eV).[52] For Fe_3O_4/GA, its O 1s spectrum can be fitted into three peaks, at 529.9, 531.5, and 532.9 eV. The peak at 532.9 eV can be attributed to the residual oxygen in graphene sheets, while the one at 529.9 eV comes from Fe_3O_4. The peak at 531.5 eV should be caused by the bonds between Fe_3O_4 and graphene and/or come from the C═O group from GO and absorbed organic groups from Fe_3O_4, because the binding energy of O in the last two conditions (about 531.3 eV) is very close to this peak. However, after annealing, most of the residual oxygen groups are eliminated, but the peak at 531.5 eV with a high area ratio (35.86%) still exists. Therefore, that the peak comes mainly from the C═O group from GO and absorbed organic groups from Fe_3O_4 is ruled out, and the peak at 531.5 eV in Fe_3O_4/GA should be attributed mainly to the Fe−O−C bond formed between graphene and Fe_3O_4.[29,52−54]

Figure 2f shows the Raman spectra of GO, GA, and Fe_3O_4/GA. The intensity ratio of D and G bands in GA and Fe_3O_4/GA was enhanced after reduction compared with that of GO. An obvious peak appears at 682 cm^{-1}, proving the presence of Fe_3O_4 nanoparticles in the graphene network. The G band shift in the carbon-based composite is related to the charge transfer between carbon and other compounds present.[52,54] Therefore, the observed G band shift by 10 cm^{-1} from 1583 cm^{-1} (graphene) to 1593 cm^{-1} (Fe_3O_4/GA) can be attributed to the charge transfer from graphene to Fe_3O_4, supporting the formation of Fe−O−C bonds between Fe_3O_4 and graphene sheets. Then it can be concluded that, during the graphene self-assembly process, Fe_3O_4 nanoparticles could be homogeneously deposited on graphene sheets by forming Fe−O−C bonds (such as $-COO^-$) between Fe_3O_4 and GO, and those nanoparticles are retained on the surface of GA by chemical attachment after anneal treatment.[29,52−54]

To study the magnetic properties of Fe_3O_4/GA, magnetic hysteresis loops were recorded at room temperature in an applied magnetic field up to 40 000 Oe, as shown in Figure 2g. The sample shows paramagnetic behavior, with a coercive force of 40.2 Oe and a remnant magnetization of 1.5 emu g^{-1} (the inset plot of Figure 2g). The saturation magnetization of Fe_3O_4/GA is 37.84 emu g^{-1}, smaller than that of the bulk magnetic Fe_3O_4 (92 emu g^{-1}),[55] which can be attributed to the presence of abundant graphene sheets in Fe_3O_4/GA (Figure S4).[29,31,56]

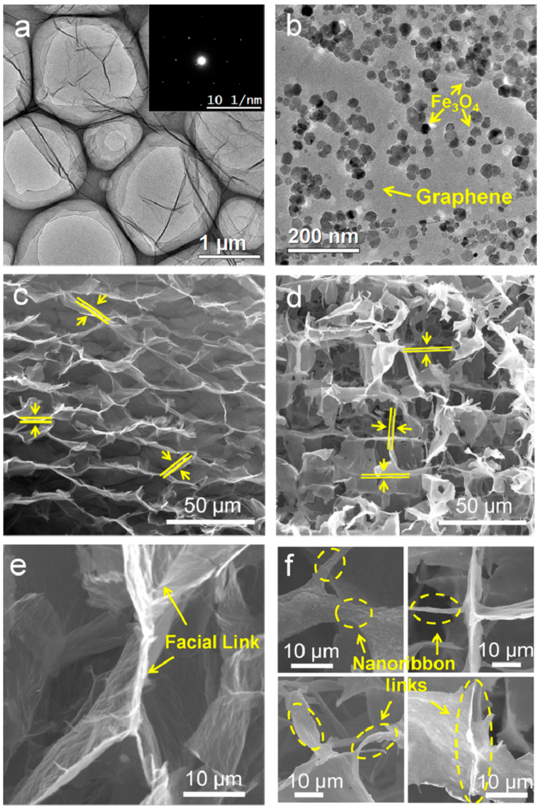

Figure 3. TEM and SEM images of the GA and Fe_3O_4/GA. (a) TEM image of GO and the diffraction pattern of a single flake (inset). (b) TEM image of Fe_3O_4 nanoparticle decorated graphene sheets. (c, d) SEM images of microporous structures of GA and Fe_3O_4/GA. (e, f) SEM images of cross-linking patterns of GA and Fe_3O_4/GA.

The morphology and structure of Fe_3O_4/GA was investigated by transmission electron microscopy (TEM) and scanning electron microscopy (SEM). Figure 3a shows that as-fabricated GO forms layers, giving a single crystal electron diffraction pattern spots. After the formation of Fe_3O_4/GA, Fe_3O_4 nanoparticles with an average size of about 30 ± 10 nm were captured and distributed homogeneously on the surface of the graphene sheets (Figure 3b and Figure S15c,d). Figures 3c and d show the SEM images of the cross-section of GA and Fe_3O_4/GA. Clearly, both aerogels possess honeycomb-like 3D porous architectures (Figures S5 and S6) with an average pore size about 30 ± 10 μm (Figure S7). These pores were shaped by the ice crystals during freezing. However, compared with GA, Fe_3O_4/GA possesses thinner pore walls and exhibits more free-hanging graphene sheets. To understand this structural difference, the cross-linking areas of GA and Fe_3O_4/GA were studied, as shown in Figure 3e,f. For GA, graphene sheets are assembled *via* a facial-linking pattern[6] (Figure 3e). While due to the Fe_3O_4 nanoparticles' decoration, the regions on graphene sheets that are available for self-assembly and

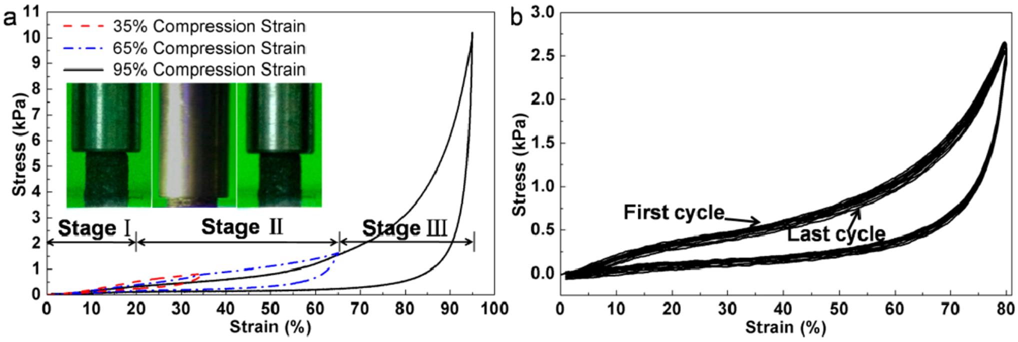

Figure 4. Mechanical compression tests of Fe_3O_4/GA. (a) The stress−strain curves of Fe_3O_4/GA at the maximum strains of 35%, 65%, and 95%, respectively. (b) The stress−strain curves of Fe_3O_4/GA at the maximum strains of 80% for 20 cycles.

van der Waals bonding are limited, leading to thinner pore walls and the nanoribbon-linking pattern for Fe_3O_4/GA (Figure 3f). These structural changes in Fe_3O_4/GA can be verified by using the Brunauer−Emmett−Teller (BET) method, as shown in Figure S8. The BET-specific surface area and pore volume of Fe_3O_4/GA are 83.07 $m^2\ g^{-1}$ and 0.25 $cm^3\ g^{-1}$, respectively, which are higher than those of GA (57.01 $m^2\ g^{-1}$ and 0.15 $cm^3\ g^{-1}$). Combining the BET results with SEM images (Figure 3c−f), the higher specific surface area and pore volume of Fe_3O_4/GA should be attributed to its thinner pore walls and the nanoribbon-linking pattern.

The mechanical properties of GA and Fe_3O_4/GA were tested using an Instron 4505 universal testing machine under quasi-static conditions (2 mm min^{-1}), as shown in Figure S9 and Figure 4a. Both of them can be compressed into a "pancake" with a very small transverse expansion and a large strain up to 95% (much higher than that of aerogels fabricated by small-area GO (Figure S10)) and recover to their original morphology after removal of the applied pressure. However, the Young's modulus of Fe_3O_4/GA is 2.3 kPa, only half that of GA (Figure S11), which is consistent with their BET results and structure shown in Figure 3e,f. From the stress−strain curves of Fe_3O_4/GA (Figure 4a), the sample compression consists of three stages: In stage I (ε from 0 to 20%) the compressive stress increases linearly with strain, indicating an elastic deformation. In stage II (ε from 20% to 65%) abundant pores of the sample are gradually compressed and a stress plateau is formed. Once the porous network is compacted, in stage III ($\varepsilon > 65\%$) the stress increases rapidly, exhibiting a typical densification process. Figure 4b shows the cyclic stress−strain curves at a strain up to 80%. It can be seen that the mechanical properties during 20 compression cycles are fairly stable, with the Young's modulus loss of 16% and residual strain of 9.8% at the 20th cycle compared with the first cycle. Thus, the as-synthesized Fe_3O_4/GA possesses excellent deformability without structural damage or collapse. Compared with other 3D carbon-based metamaterials (Figure S12),[9,19,57−59] which exhibit 10−100 mg cm^{-3} density, 0.02−100 MPa ultimate stress, and 60−90% compressive strain, Fe_3O_4/GA shows a lower ultimate stress but larger compressive strain, indicating an easier actuation. Energy dissipation capability of the magnetic aerogels is measured by the area under the stress−strain curve. The energy density of Fe_3O_4/GA with 80% strain is about 4.5 J g^{-1}, much larger than the traditional damping materials.[60]

The magnetic actuation of Fe_3O_4/GA was studied under a solenoid-generated uniform magnetic field, as shown in Figure 5a. The samples are put on the iron core horizontally and vertically to test their magnetic field-induced deformation behavior in the radial and axial direction. For the radial direction (Figure 5b), a large compressive strain, up to 25%, can be obtained even at a low magnetic intensity (about 0.1 T). The compressive strain increases with the growth of the magnetic intensity, and finally, due to the magnetic saturation of the Fe_3O_4 nanoparticles, compressive strain reaches its maximum value of about 52.3%. As the magnetic intensity decreases at the same rate, Fe_3O_4/GA begins to unfold and finally recovers to its original morphology. For the axial direction, Fe_3O_4/GA shows a similar compressive behavior under the magnetic field, while only 7.6% strain is obtained at 0.1 T and 35.3% maximum strain at 1.2 T. This different compressibility of Fe_3O_4/GA along the axial and radial directions may be attributed to the anisotropic pore structures (Figure 3c,d) and different distances from the iron core.

The dynamics of deformation of Fe_3O_4/GA under magnetic fields is reported in Figure S13. With a constant rate of change in magnetic field intensity (0.08 T s^{-1}), Fe_3O_4/GA performs up to a 13.69% s^{-1} rate of change in deformation strain, indicating a rapid response (a detailed discussion is provided in the Supporting Information). The relationship between the deformation behavior of Fe_3O_4/GA and the strength of the magnetic field is studied by a mathematic fitting method. The experimental data can be well fitted by the logarithmic equation, indicating an approximate logarithmic relationship between them (fitting details are provided in the Supporting Information and Figure S14).

Furthermore, obvious stiffening can be observed from the field-induced compression, marked by the

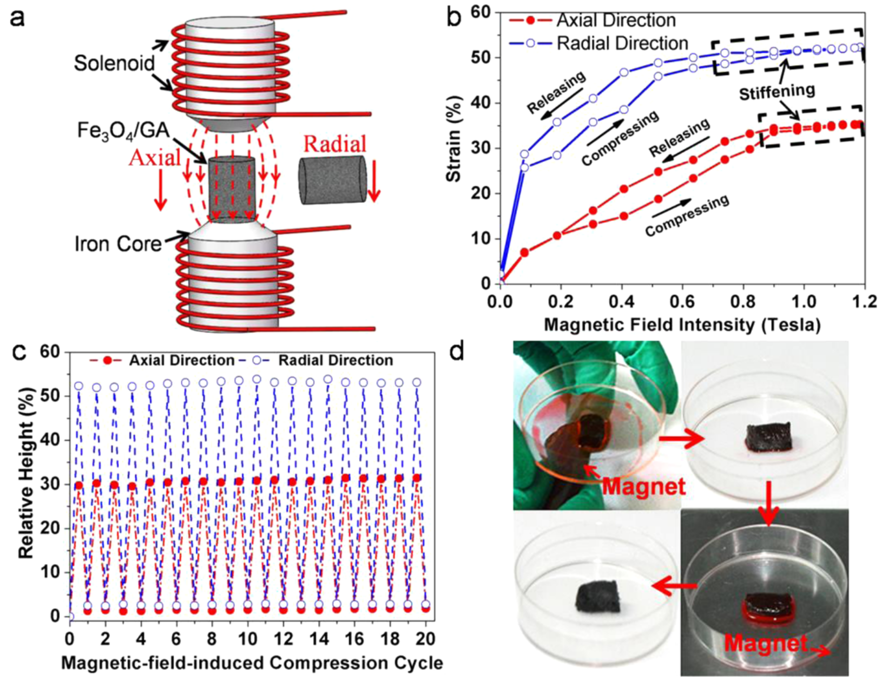

Figure 5. Magnetic actuation tests of Fe_3O_4/GA. (a) Diagram of the experimental setup for the magnetic actuation testing. (b) Field-induced strains as a function of the magnetic field intensity. (c) Variation of sample heights along the axial and radial direction for 20 field-induced deformation cycles. (d) Remote control of Fe_3O_4/GA for oil absorption and recycle: Fe_3O_4/GA can be guided by a magnet to move to absorb oil. After saturation, oil can be released from Fe_3O_4/GA by magnetic field-induced compression. The regenerated aerogels still keep their original shapes.

black dotted lines in Figure 5b, which can be attributed to the action of magnetic torques caused by the magnetic orientation on the Fe_3O_4/GA. This interesting phenomenon can be used to enhance the output force of the magnetic aerogel, which will be studied in the future. The recoverability of field-induced deformation was tested as shown in Figure 5c. Fe_3O_4/GA shows a stable deformability during 20 loading−unloading cycles, and no obvious residual strain was induced by the magnetic force, demonstrating an excellent magnetic actuation characteristic. The morphology and amount of Fe_3O_4 on GA after the deformation test in a 1 T magnetic field were examined by SEM and TEM (Figure S15). Compared to its original condition, no obvious detachment or aggregation of Fe_3O_4 happened, which can be attributed to the strong Fe−O−C bonds between Fe_3O_4 nanoparticles and graphene sheets. On the basis of this characteristic, Fe_3O_4/GA can be applied for oil absorption and recycling, as shown in Figure 5d. About 8 mg of Fe_3O_4/GA can completely absorb 1.2 g of gasoline remotely controlled by a magnet, and most of the absorbed liquid can be recycled from Fe_3O_4/GA by applying magnetic field-induced compression, which is more practical than the mechanical extrusion method.

As the 3D network of Fe_3O_4/GA is assembled by restoring the conjugation of sp^2 regions and $\pi-\pi$ stacking interactions between 2D graphene sheets, the electrical resistance of Fe_3O_4/GA may be deformation-dependent, which inspires a possible self-sensing property. Figure 6a shows the $I-V$ curve of Fe_3O_4/GA and the aerogel exhibits an ohmic characteristic with a conductivity of about 0.348 S cm^{-1}, a little less than that of GA (about 0.412 S cm^{-1} in Figure S16). This poorer conductivity of Fe_3O_4/GA can also be attributed to the influence of Fe_3O_4 nanoparticles, separating some of the graphene sheets. The thermal stability of the conductivity was tested (the inset plot of Figure 6a), and it is observed that the conductivity of Fe_3O_4/GA can be maintained at about 0.3 S cm^{-1} from 0 to 40 °C, while raising or decreasing the temperature by 20 °C increases the conductivity to its maximum value of about 0.541 S cm^{-1}. Figure 6b shows the variation in electrical resistance of Fe_3O_4/GA caused by the magnetic field-induced deformation. As the magnetic field intensity is increased from 0 to 1 T, high compressive strains of 30% and 50% are achieved along the axial and radial directions, respectively, leading to a 35% and 53% decrease in the electrical resistance, respectively. The resistance variations are almost linearly proportional to the deformation strains, while a slight hysteresis can be observed during the radial compression−release tests, which may be attributed to the additional action of magnetic torques caused by the magnetic orientation effects on Fe_3O_4 nanoparticles.

To illustrate the mechanism of electrical resistance variation of Fe_3O_4/GA caused by the deformation, the structure changes of Fe_3O_4/GA before and under 50% deformation were examined by SEM, as shown in Figure 6c. Before deformation, Fe_3O_4/GA shows a

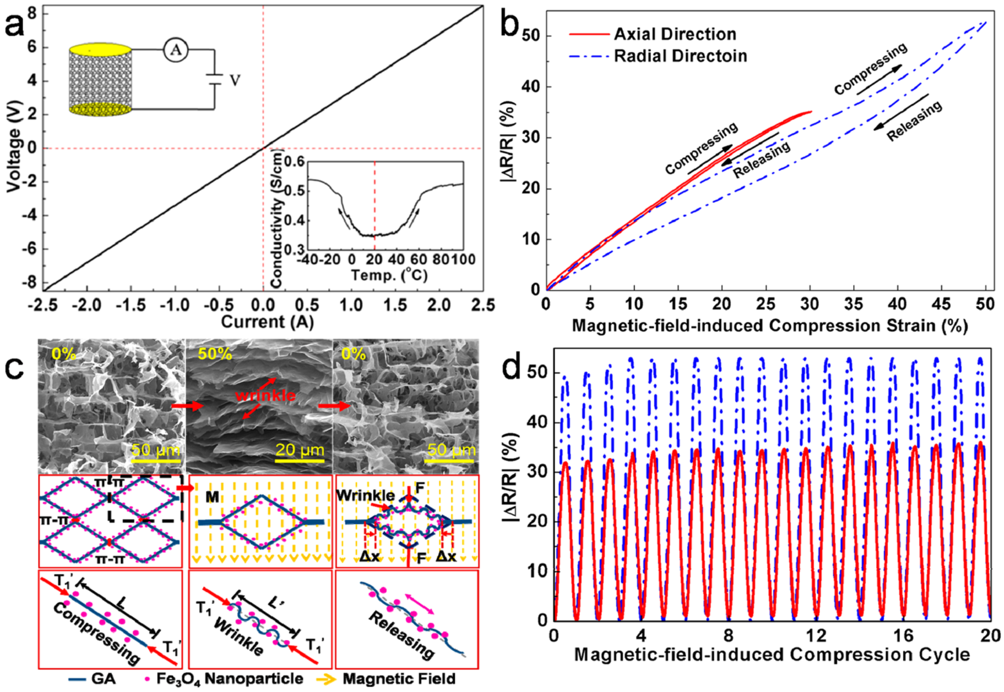

Figure 6. Electronic properties of Fe_3O_4/GA. (a) *I*−*V* curve of the aerogels and thermal stability of its conductivity for the inset plot. (b) Variations of the electrical resistance of Fe_3O_4/GA as a function of the magnetic field-induced deformation. (c) Illustration of the mechanism of strain-dependent electrical resistance of Fe_3O_4/GA. (d) Variation of the resistance for 20 cycles.

regular 3D porous architecture, leading to a conductivity of about 0.348 S cm^{-1}. While under 50% deformation, pores of the sample are gradually compressed and the cell walls are wrinkled, as depicted in Figure 6c. As a result, the stacking areas of graphene sheets between cell walls are increased during the compressive process, resulting in more pathways for electron transport.[14,18,19,61] Once the external pressure is removed, the Fe_3O_4/GA unfolds almost completely, and its electrical resistance recovers to the original value.

Figure 6d shows the variation stability of the electrical resistance under cyclic magnetic actuation. During 20 compression cycles, the resistance shows a stable and synchronous response to the strain. Thus, the field-induced deformation of Fe_3O_4/GA can be monitored in real time by measuring the variations of electrical resistance, enabling applications of this material in self-sensing soft actuators and microswitches.

CONCLUSIONS

We have fabricated an ultralight magnetic elastomer based on the graphene aerogel homogeneously decorated with Fe_3O_4 nanoparticles. This ultralight Fe_3O_4/GA is the lightest magnetic elastomer ever reported. The magnetic aerogel exhibits excellent controllability, actuation, and reversible deformation as well as large field-induced strain and strain-dependent electrical resistance. Those properties make this elastomer useful for applications in self-sensing soft actuators, microsensors and microswitches, remotely controlled oil absorption, and recycling. This work provides a general strategy for fabricating lightweight inorganic elastomers for a variety of applications.

EXPERIMENTAL SECTION

Preparation of 3D Fe_3O_4/GA. GO was prepared *via* a modified Hummers method.[62,63] The magnetic Fe_3O_4 nanoparticles were fabricated by a typical chemical co-precipitation method.[64] Then, 0.01−0.2 mmol of Fe_3O_4 nanoparticles were homogeneously dispersed into 10 mL of as-fabricated GO or commercial GO (∼1 μm in area, TimesGraph) suspension (2 mg mL^{-1}) by mild ultrasonication for 30 min. Next, 30 μL of ethylenediamine was added as assistant reducing agent, and the mixture was ultrasonically dispersed in an ice bath for 1 h. Then, 2.5 mL of the mixture was placed in a 5 mL vial and maintained at 120 °C in a 25 mL Teflon-lined autoclave for 2 h. After that, the autoclave was naturally cooled to room temperature and the as-formed hydrogel was poured out and dialyzed with 1 L of solvent composed of distilled water and ethanol with a volume ratio of 5:1 for 24 h. Last, the hydrogel was frozen at −80 °C for 24 h and then freeze-dried into the areogel. The Fe_3O_4/GA samples were annealed at 250 °C for 1 h to reduce the assembled graphene by partially eliminating the functional groups. By testing the magnetic actuation response of Fe_3O_4/GA with different nanoparticle loading, it was determined that 0.1 mmol of Fe_3O_4 was the optimal loading for 20 mg of GO.

Conflict of Interest: The authors declare no competing financial interest.

Supporting Information Available: Materials, characterization details, additional figures, and videos. This material is available free of charge *via* the Internet at http://pubs.acs.org.

Acknowledgment. This research was supported by the Ministry of Science and Technology, China (Grant No. 2011BAK02B02). Collaboration between Drexel University and Dalian University of Technology was supported by the Cheung Kong Scholarship.

REFERENCES AND NOTES

1. Nardecchia, S.; Carriazo, D.; Ferrer, M. L.; Gutierrez, M. C.; del Monte, F. Three Dimensional Macroporous Architectures and Aerogels Built of Carbon Nanotubes and/or Graphene: Synthesis and Applications. *Chem. Soc. Rev.* **2013**, *42*, 794–830.
2. Liu, L.; Ma, W.; Zhang, Z. Macroscopic Carbon Nanotube Assemblies: Preparation, Properties, and Potential Applications. *Small* **2011**, *6*, 1505–1517.
3. Zhu, Y.; Murali, S.; Cai, W.; Li, X.; Suk, J. W.; Potts, J. R.; Ruoff, R. S. Graphene and Graphene Oxide: Synthesis, Properties, and Applications. *Adv. Mater.* **2010**, *15*, 3906–3923.
4. Jiang, L.; Fan, Z. Design of Advanced Porous Graphene Materials: From Graphene Nanomesh to 3D Architectures. *Nanoscale* **2014**, *21*, 1922–1945.
5. Sun, X.; Sun, H.; Li, H.; Peng, H. Developing Polymer Composite Materials: Carbon Nanotubes or Graphene. *Adv. Mater.* **2013**, *4*, 5153–5176.
6. Xu, Y.; Sheng, K.; Li, C.; Shi, G. Self-Assembled Graphene Hydrogel *via* a One-Step Hydrothermal Process. *ACS Nano* **2010**, *4*, 4324–4330.
7. Huang, Y.; Liang, J.; Chen, Y. An Overview of the Applications of Graphene-Based Materials in Supercapacitors. *Small* **2012**, *25*, 1805–1839.
8. Ghosh, A.; Lee, Y. H. Carbon-Based Electrochemical Capacitors. *ChemSusChem* **2012**, *12*, 480–579.
9. Gui, X. C.; Cao, A. Y.; Wei, J. Q.; Li, H. B.; Jia, Y.; Li, Z.; Fan, L. L.; Wang, K. L.; Zhu, H. W.; Wu, D. H. Soft, Controlled Compressibility, Highly Conductive Nanotube Sponges and Composites. *ACS Nano* **2010**, *4*, 2320–2326.
10. Fowler, J. D.; Allen, M. J.; Tung, V. C.; Yang, Y.; Kaner, R. B.; Weiller, B. H. Practical Chemical Sensors from Chemically Derived Graphene. *ACS Nano* **2009**, *3*, 301–306.
11. Das, B.; Choudhury, B.; Gomathi, A.; Manna, A. K.; Pati, S. K.; Rao, C. N. R. Interaction of Inorganic Nanoparticles with Graphene. *ChemPhysChem* **2011**, *12*, 937–943.
12. Zhao, Y.; Hu, C. G.; Hu, Y.; Cheng, H. H.; Shi, G. Q.; Qu, L. T. A Versatile, Ultralight, Nitrogen-Doped Graphene Framework. *Angew. Chem., Int. Ed.* **2012**, *51*, 11533–11537.
13. Chen, Z.; Xu, C.; Ma, C.; Ren, W.; Cheng, H. Lightweight and Flexible Graphene Foam Composites for High-Performance Electromagnetic Interference Shielding. *Adv. Mater.* **2013**, *25*, 1296–1300.
14. Li, J.; Li, J.; Meng, H.; Xie, S.; Zhang, B.; Li, L.; Ma, H.; Zhang, J.; Yu, M. Ultra-Light, Compressible and Fire-Resistant Graphene Aerogel as a Highly Efficient and Recyclable Absorbent for Organic Liquids. *J. Mater. Chem. A* **2014**, *2*, 2934–2941.
15. Nguyen, D. D.; Tai, N. H.; Lee, S. B.; Kuo, W. S. Superhydrophobic and Superoleophilic Properties of Graphene-Based Sponges Fabricated Using a Facile Dip Coating Method. *Energy Environ. Sci.* **2012**, *5*, 7908–7912.
16. Schaedler, T. A.; Jacobsen, A. J.; Torrents, A.; Sorensen, A. E.; Lian, J.; Greer, J. R.; Valdevit, L.; Carter, W. B. Ultralight Metallic Microlattices. *Science* **2011**, *334*, 962–965.
17. Kim, K. H.; Oh, Y.; Islam, M. F. Graphene Coating Makes Carbon Nanotube Aerogels Superelastic and Resistant to Fatigue. *Nat. Nanotechnol.* **2012**, *7*, 562–567.
18. Sun, H.; Xu, Z.; Gao, C. Multifunctional, Ultra-Flyweight, Synergistically Assembled Carbon Aerogels. *Adv. Mater.* **2013**, *25*, 2554–2560.
19. Hu, H.; Zhao, Z.; Wan, W.; Gogotsi, Y.; Qiu, J. Ultralight and Highly Compressible Graphene Aerogels. *Adv. Mater.* **2013**, *25*, 2219–2223.
20. Chen, Z.; Ren, W.; Gao, L.; Liu, B.; Pei, S.; Cheng, H. Three-Dimensional Flexible and Conductive Interconnected Graphene Networks Grown by Chemical Vapour Deposition. *Nat. Mater.* **2011**, *10*, 424–428.
21. Bi, H.; Xie, X.; Yin, K.; Zhou, Y.; Wan, S.; He, L.; Xu, F.; Banhart, F.; Sun, L.; Ruoff, R. S. Spongy Graphene as A Highly Efficient and Recyclable Sorbent for Oils and Organic Solvents. *Adv. Funct. Mater.* **2012**, *22*, 4421–4425.
22. Chen, W. F.; Yan, L. F. *In Situ* Self-Assembly of Mild Chemical Reduction Graphene for Three-Dimensional Architectures. *Nanoscale* **2011**, *3*, 3132–3137.
23. Kim, S.; Pham, H. D.; Pham, V. H.; Cuong, T. V.; Nguyen-Phan, T. D.; Chung, J. S.; Shin, E. W. Synthesis of The Chemically Converted Graphene Aerogel with Superior Electrical Conductivity. *Chem. Commun.* **2011**, *47*, 9672–9674.
24. Zhang, X. T.; Sui, Z. Y.; Xu, B.; Yue, S. F.; Luo, Y. J.; Zhan, W. C.; Liu, B. Mechanically Strong and Highly Conductive Graphene Aerogel and Its Use as Electrodes for Electrochemical Power Sources. *J. Mater. Chem.* **2011**, *21*, 6494–6497.
25. Worsley, M. A.; Olson, T. Y.; Lee, J. R. I.; Willey, T. M.; Nielsen, M. H.; Roberts, S. K.; Pauzauskie, P. J.; Biener, J.; Satcher, J. H.; Baumann, T. F. High Surface Area, sp^2-Cross-Linked Three-Dimensional Graphene Monoliths. *J. Phys. Chem. Lett.* **2011**, *2*, 921–925.
26. Suzuki, M.; Hanabusa, K. Polymer Organogelators That Make Supramolecular Organogels through Physical Cross-Linking and Self-Assembly. *Chem. Soc. Rev.* **2010**, *39*, 455–463.
27. Sheng, K.; Sun, Y.; Li, C.; Yuan, W.; Shi, G. Ultrahigh-Rate Supercapacitors Based on Electrochemically Reduced Graphene Oxide for as Line-Filtering. *Sci. Rep.* **2012**, *2*, 247–251.
28. Qiu, L.; Liu, J. Z.; Chang, S. L.; Wu, Y.; Li, D. Biomimetic Superelastic Graphene-Based Cellular Monoliths. *Nat. Commun.* **2012**, *3*, 1241–1247.
29. Chen, W.; Li, S.; Chen, C.; Yan, L. Self-Assembly and Embedding of Nanoparticles by *in Situ* Reduced Graphene for Preparation of a 3D Graphene/Nanoparticle Aerogel. *Adv. Mater.* **2011**, *23*, 5679–5683.
30. Wang, R.; Xu, C.; Sun, J.; Gao, L. Three-Dimensional Fe$_2$O$_3$ Nanocubes/Nitrogen-Doped Graphene Aerogels: Nucleation Mechanism and Lithium Storage Properties. *Sci. Rep.* **2014**, *4*, 7171.
31. Cong, H.; Ren, X.; Wang, P.; Yu, S. Macroscopic Multifunctional Graphene-Based Hydrogels and Aerogels by a Metal Ion Induced Self-Assembly Process. *ACS Nano* **2012**, *6*, 2693–2703.
32. Wu, Z.; Yang, S.; Sun, Y.; Parvez, K.; Feng, X.; Müllen, K. 3D Nitrogen-Doped Graphene Aerogel-Supported Fe$_3$O$_4$ Nanoparticles as Efficient Electrocatalysts for the Oxygen Reduction Reaction. *J. Am. Chem. Soc.* **2012**, *134*, 9082–9085.
33. Yin, H.; Zhang, C.; Liu, F.; Hou, Y. Hybrid of Iron Nitride and Nitrogen-Doped Graphene Aerogel as Synergistic Catalyst for Oxygen Reduction Reaction. *Adv. Funct. Mater.* **2014**, *24*, 2930–2937.
34. Ren, L.; Hui, K. S.; Hui, K. N. Self-Assembled Free-Standing Three-Dimensional Nickel Nanoparticle/Graphene Aerogel for Direct Ethanol Fuel Cells. *J. Mater. Chem. A* **2013**, *1*, 5689–5694.
35. Dubey, S. P.; Dwivedi, A. D. Synthesis of Graphene−Carbon Sphere Hybrid Aerogel with Silver Nanoparticles and Its Catalytic and Adsorption Applications. *Chem. Eng. J.* **2014**, *244*, 160–167.
36. Zhang, J.; Li, R.; Li, Z.; Liu, J.; Gu, Z.; Wang, G. Synthesis of Nitrogen-Doped Activated Graphene Aerogel/Gold Nanoparticles and Its Application for Electrochemical Detection of Hydroquinone and *o*-Dihydroxybenzene. *Nanoscale* **2014**, *6*, 5458–5466.
37. Liu, X.; Cui, J.; Sun, J.; Zhang, X. 3D Graphene Aerogel-Supported SnO$_2$ Nanoparticles for Efficient Detection of NO$_2$. *RSC Adv.* **2014**, *4*, 22601–22605.
38. Jiang, H.; Li, C.; Huang, X. Actuators Based on Liquid Crystalline Elastomer Materials. *Nanoscale* **2013**, *21*, 5225–5240.
39. Khoo, M.; Liu, C. Micro Magnetic Silicone Elastomer Membrane Actuator. *Sens. Actuators, A: Phys.* **2001**, *89*, 259–266.
40. Zhao, X.; Kim, J.; Cezar, C. A.; Huebsch, N.; Lee, K.; Bouhadir, K.; Mooney, D. J. Active Scaffolds for on-Demand Drug and Cell Delivery. *Proc. Natl. Acad. Sci. U.S.A.* **2011**, *108*, 67–73.

41. Skaat, H.; Ziv-Polat, O.; Shahar, A.; Last, D.; Mardor, Y.; Margel, S. Magnetic Scaffolds Enriched with Bioactive Nanoparticles for Tissue Engineering. *Adv. Healthcare Mater.* **2012**, *1*, 168–171.
42. Sapir, Y.; Cohen, S.; Friedman, G.; Polyak, B. The Promotion of *in Vitro* Vessel-Like Organization of Endothelial Cells in Magnetically Responsive Alginate Scaffolds. *Biomaterials* **2012**, *33*, 4100–4109.
43. Evans, B. A.; Fiser, B. L.; Prins, W. J.; Rapp, D. J.; Shields, A. R.; Glass, D. R.; Superfine, R. A Highly Tunable Silicone-Based Magnetic Elastomer with Nanoscale Homogeneity. *J. Magn. Magn. Mater.* **2012**, *324*, 501–507.
44. Li, Y.; Huang, G.; Zhang, X.; Li, B.; Chen, Y.; Lu, T.; Lu, T. J.; Xu, F. Magnetic Hydrogels and Their Potential Biomedical Applications. *Adv. Funct. Mater.* **2013**, *23*, 660–672.
45. Kornev, K. G.; Halverson, D.; Korneva, G.; Gogotsi, Y.; Friedman, G. Magnetostatic Interactions between Carbon Nanotubes Filled with Magnetic Nanoparticles. *Appl. Phys. Lett.* **2008**, *92*, 233117–3.
46. Korneva, K. G.; Ye, H.; Gogotsi, Y.; Halverson, D.; Friedman, G.; Bradley, J. C.; Kornev, K. G. Carbon Nanotubes Loaded with Magnetic Particles. *Nano Lett.* **2005**, *5*, 879–884.
47. Korobeinyk, A. V.; Whitby, R. L. D.; Niu, J. J.; Gogotsi, Y.; Mikhalovsky, S. V. Rapid Assembly of Carbon Nanotube-Based Magnetic Composites. *Mater. Chem. Phys.* **2011**, *128*, 514–518.
48. Fuhrer, R.; Athanassiou, E.; Luechinger, N.; Stark, W. Cross-linking Metal Nanoparticles into the Polymer Backbone of Hydrogels Enables Preparation of Soft, Magnetic Field-Driven Actuators with Muscle-Like Flexibility. *Small* **2009**, *5*, 383–388.
49. Olsson, R.; Samir, M.; Salazar-Alvarez, G.; Belova, L.; Ström, V.; Berglund, L.; Ikkala, O.; Nogués, J.; Gedde, U. Making Flexible Magnetic Aerogels and Stiff Magnetic Nanopaper Using Cellulose Nanofibrils as Templates. *Nat. Nanotechnol.* **2010**, *5*, 584–588.
50. Ramanujan, R.; Lao, L. The Mechanical Behavior of Smart Magnet−Hydrogel Composites. *Smart Mater. Struct.* **2006**, *15*, 952–956.
51. Dikin, D. A.; Stankovich, S.; Zimney, E. J.; Piner, R.; Dommett, G. H. B.; Evmenenko, G.; Nguyen, S. T.; Ruoff, R. S. Preparation and Characterization of Graphene Oxide Paper. *Nature* **2007**, *448*, 457–460.
52. Zubir, N.; Yacou, C.; Motuzas, J.; Zhang, X.; Costa, J. Structural and Functional Investigation of Graphene Oxide−Fe_3O_4 Nanocomposites for the Heterogeneous Fenton-like Reaction. *Sci. Rep.* **2014**, *4*, 4594.
53. Zhou, G.; Wang, D.; Yin, L.; Li, N.; Li, F.; Cheng, H. Oxygen Bridges between NiO Nanosheets and Graphene for Improvement of Lithium Storage. *ACS Nano* **2012**, *6*, 3214–3222.
54. Zhou, J.; Song, H.; Ma, L.; Chen, X. Magnetite/Graphene Nanosheet Composites: Interfacial Interaction and Its Impact on the Durable High-Rate Performance in Lithium-Ion Batteries. *RSC Adv.* **2011**, *1*, 782–791.
55. Gao, M. R.; Zhang, S. R.; Jiang, J.; Zheng, Y. R.; Tao, D. Q.; Yu, S. H. One-Pot Synthesis of Hierarchical Magnetite Nanochain Assemblies with Complex Building Units and Their Application for Water Treatment. *J. Mater. Chem.* **2011**, *21*, 16888–16892.
56. Chandra, V.; Park, J.; Chun, Y.; Lee, J.; Hwang, I.; Kim, K. Water-Dispersible Magnetite-Reduced Graphene Oxide Composites for Arsenic Removal. *ACS Nano* **2010**, *4*, 3979–3986.
57. Zhang, Q.; Zhao, M.; Liu, Y.; Cao, A.; Qian, W.; Lu, Y.; Wei, F. Energy-Absorbing Hybrid Composites Based on Alternate Carbon-Nanotube and Inorganic Layers. *Adv. Mater.* **2009**, *21*, 2876–2880.
58. Gui, X.; Zeng, Z.; Zhu, Y.; Li, H.; Lin, Z.; Gan, Q.; Xiang, R.; Cao, A.; Tang, Z. Three-Dimensional Carbon Nanotube Sponge-Array Architectures with High Energy Dissipation. *Adv. Mater.* **2014**, *26*, 1248–1253.
59. Tang, C.; Zhang, Q.; Zhao, M.; Tian, G.; Wei, F. Resilient Aligned Carbon Nanotube/Graphene Sandwiches for Robust Mechanical Energy Storage. *Nano Energy* **2014**, *7*, 161–169.
60. Surani, F. B.; Kong, X.; Qiao, Y. Two-Staged Sorption Isotherm of a Nanoporous Energy Absorption System. *Appl. Phys. Lett.* **2005**, *87*, 251906–3.
61. Wu, Y.; Yi, N.; Huang, L.; Zhang, T.; Fang, S.; Chang, H.; Li, N.; Oh, J.; Lee, J.; Kozlov, M.; *et al.* Three-Dimensionally Bonded Spongy Graphene Material with Super Compressive Elasticity and Near-Zero Poisson's Ratio. *Nat. Commun.* **2015**, *6*, 6141.
62. Gilje, S.; Han, S.; Wang, M.; Wang, K. L.; Kaner, R. B. A Chemical Route to Graphene for Device Applications. *Nano Lett.* **2007**, *7*, 3394–3398.
63. Xu, Z.; Sun, H. Y.; Zhao, X. L.; Gao, C. Ultrastrong Fibers Assembled from Giant Graphene Oxide Sheets. *Adv. Mater.* **2013**, *25*, 188–193.
64. Kang, Y. S.; Risbud, S.; Rabolt, J. F.; Stroeve, P. Synthesis and Characterization of Nanometer-Size Fe_3O_4 and γ-Fe_2O_3 Particles. *Chem. Mater.* **1996**, *8*, 2209–2211.